

Cold-formed Stainless Steel RHSs/SHSs under Combined Compression and Cyclic Bending

Cheng Fang, Feng Zhou, Chenhao Luo

Department of Structural Engineering, School of Civil Engineering, Tongji University, Shanghai, China

Abstract

This paper discusses the behaviour of stainless steel rectangular and square hollow sections (RHSs and SHSs) under combined constant compression and uniaxial cyclic bending. A total of 10 specimens were tested, covering a variety of section slenderness, axial load ratio, and bending direction. These test parameters were found to have evident influences on the local buckling resistance of the specimens. It was also observed that the current codified classification limits underestimate the ability of the stainless steel sections to develop plastic stresses. Moreover, the specimens exhibited low to moderate levels of ductility and energy dissipation capacity due to a relatively early occurrence of local buckling. A numerical study was subsequently conducted, shedding further light on the strength, stress pattern, ductility, and local failure behaviour of the specimens. A more extensive parametric study was then carried out, which provides basis for the proposal of a ductility-oriented design approach that aims to offer a quick yet reliable evaluation tool for predicting the available ductility supply of stainless steel RHSs/SHSs under different loading conditions. The rationality of the current major design codes for predicting the strength of stainless steel members was also evaluated, and it was found that the design codes tend to be conservative.

Keywords

Stainless steel; hollow sections; local buckling; cyclic loading; hysteretic response; ductility.

1 Introduction

Owing to favourable corrosion resistance, workability, ductility, and aesthetic appearance, stainless steel has now been considered as a viable class of constructional material to cater to both architectural and structural needs. Compared with low carbon steel, stainless steel exhibits a distinctive nonlinear stress-strain relationship with relatively low proportional limit, no strictly defined yield plateau, and evident strain hardening. These properties can result in different behaviours between stainless steel and low carbon steel members. Over the past two decades, extensive investigations have been conducted on stainless steel at material, cross-section and member levels. The applicability of the existing structural steel design principles to stainless steel structures has been carefully revisited, and modifications or new design approaches have been proposed where necessary. A number of early research outcomes have already been included in major stainless steel design codes^{1,2,3}, which further promoted widespread applications of this material in buildings and infrastructures, including Louvre Pyramid (France), Millennium footbridge (UK), and Tsing Ma Bridge (Hong Kong)⁴.

So far, most of the relevant studies focused on the behaviour of stainless steel members under static loading conditions. At section level, Young and Lui⁵ conducted a series of compression tests on stainless steel square and rectangular hollow section (SHS and RHS) stub columns, and it was concluded that the design predictions for section capacity are generally conservative. Gardner and Nethercot⁶ carried out 37 more tests on such columns, based on which a new design approach was proposed. Bardi and Kyriakides⁷ examined a number of stainless steel circular hollow sections (CHSs), where the focus was given to the inelastic local buckling behaviour. Zhou et al.⁸ discussed the interaction effect of constituent plate elements within stainless steel cross-sections, and found that the interaction effect is quite obvious particularly for slender sections. Summarising available test data, design recommendations on stainless steel section classifications were given by Gardner and Theofanous⁹.

Apart from the tests and analysis on stub columns, slender stainless steel columns were investigated by Rasmussen and Hancock¹⁰, Young and Liu¹¹, Liu and Young¹², and Theofanous and Gardner¹³. It was commonly found that the current flexural buckling curve for stainless steel hollow section columns is generally accurate, although for certain column types under specific boundary conditions (e.g. fixed-ended cold-formed stainless steel RHS/SHS columns), the design capacities predicted by the American and European codes^{1,2} can be less reliable than those predicted by the Australian/New Zealand Standard³. It is noted that most of these investigations also involved stub column tests for comparison purposes, which largely enriched the test data pool for the evaluation of the section behaviour. In parallel with the studies on columns, a series of three and four point bending tests have been conducted on stainless steel RHS/SHS beams to understand their moment-curvature relationships^{14,15,16}. Recent research interests have also been extended to the behaviour of stainless steel beam-columns which were compressed with varying loading eccentricities^{17,18,19,20,21,22}. A common finding was that the current design approaches are reasonably safe, although some shortcomings related to inaccurate interaction factors have been identified. In light of this, modifications to the existing design rules were proposed²³. Furthermore, concrete-filled stainless steel tubular columns, combining the advantages of stainless steel and steel-concrete composite action, have attracted great attention^{24,25,26,27,28}. The cross-section and member responses of the composite columns under ambient and elevated temperature scenarios were covered in these studies.

The literature shows that a series of studies have been conducted on stainless steel members under monotonic static loading scenarios; however, information on their seismic performance is rare, which hinders a confident use of stainless steel members in seismic-active regions. In particular, when stainless steel is employed for columns, the cyclic performance of the column sections under combined compression and cyclic bending is of fundamental importance to structural engineers. Although some studies have been carried out to understand the basic material properties of stainless steel under cyclic loading^{29,30}, the investigations at section and member levels is generally inadequate. In light of this, the current study aims to investigate the structural behaviour of stainless steel RHSs/SHSs under cyclic loading. The research commences with an experimental study covering a various combination of section dimensions and loading scenarios. A numerical study is subsequently conducted, shedding further light on the strength, ductility, and local failure behaviour of the considered specimens. The calibrated models enable a further parametric study to be conducted taking account of a wider range of parameter matrix, and based on the available data, the codified prediction of the strength of stainless steel RHS/SHS beam-columns is commented, and a ductility-oriented design approach for these sections under seismic conditions is finally proposed.

2 Experimental Program

2.1 Test specimens

A total of 10 cold-formed stainless steel tubular section specimens were tested under constant axial load and cyclically increased uniaxial bending, as illustrated in Fig. 1. These specimens were designed as stub columns with a nominal total length (L) of 660 mm, such that overall flexural buckling can be avoided whereas local failure modes govern. The tubes were cold-rolled from Grade 304 Austenite stainless steel plates to form the desired RHS/SHS shape at room temperature and were finished by longitudinal welding. The tubes were then cut and machined to the required length. Two Q345 (nominal yield strength = 345 MPa) steel endplates with a thickness of 20 mm were welded to the two ends of each specimen, and additional stiffeners were used to strengthen the column ends. The height of each stiffener was 80 mm, leading to a reduced effective length of 500 mm for the stub columns.

The main test parameters were section dimension, axial load ratio, and bending direction. Three different section sizes were selected, namely, SHS 120×120×3, RHS 120×60×3, and RHS 120×60×2, which are abbreviated as S1, R1, and R2 sections, respectively. Details of the specimens are provided in Fig. 1 with the measured dimensions given in Table 1. The definition of the symbols for the section is marked in the figure, where b and h are the overall width of the web and that of the flange, respectively; b_p and h_p are the corresponding widths excluding the rounded corners; t is the thickness of the tube, r_0 is the outer radius of the arc corner, and V shows the loading/bending direction. Since local buckling is the main concern of the current study, relatively slender sections were selected for the specimens. The measured width-to-thickness ratios, i.e., $r_f = h_p/\epsilon t$ and $r_w = b_p/\epsilon t$, ranged from 24.7 to 85.4, where $\epsilon = (235E_0/210000\sigma_{0.2})^{0.5}$, in which E_0 is the measured Young's modulus, and $\sigma_{0.2}$ is the measured yield strength (0.2% proof stress) of the flat part, as elaborated later. Two different levels of axial load ratio (n) were considered in the tests, i.e., $n = 0.2$ and $n = 0.4$, where $n = P/\sigma_{0.2}A$, in which P is the applied constant axial load, and A is the measured cross-sectional area. Both strong-axis and weak-axis bending scenarios were considered for the specimens. For ease of reference, each specimen was designated with a specimen code, starting with the section type, followed by the axial load ratio (n), and ending with the bending direction (S = Strong axis bending and W = Weak axis bending).

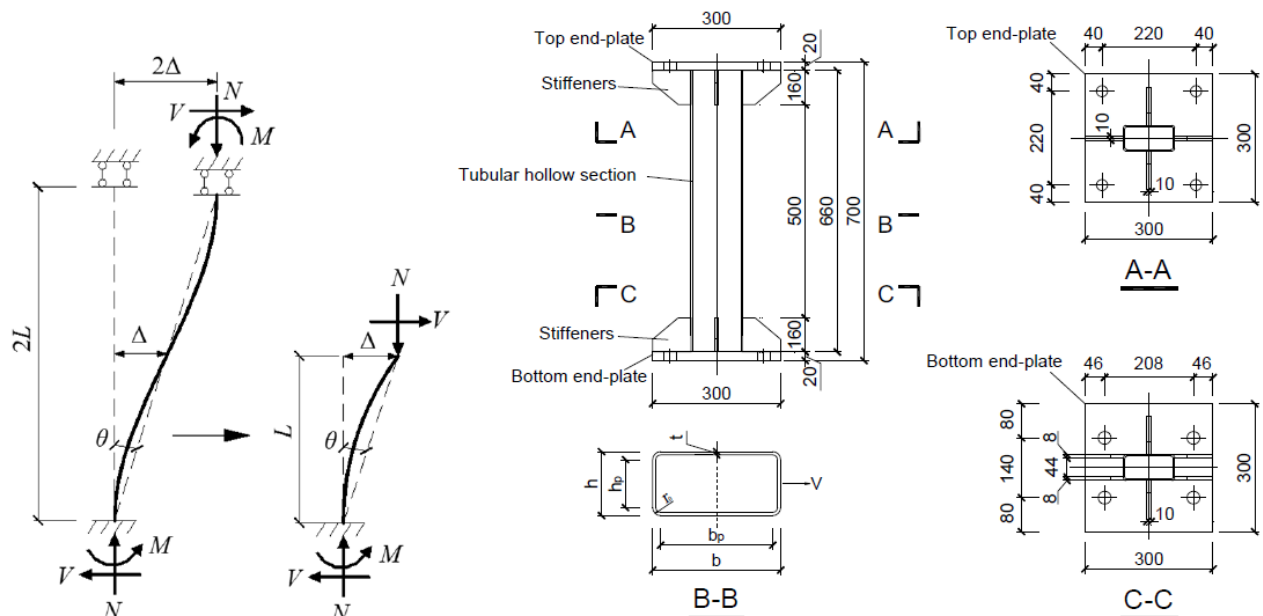


Fig. 1 Details of test specimens**Table 1 Measured dimensions and loading details of specimens**

Specimens	b (mm)	h (mm)	t (mm)	r_0 (mm)	r_t	r_w	n	Bending direction
S1-n0.2	120.52	120.24	2.81	7.03	50.1	50.3	0.20	-
S1-n0.4	120.52	120.24	2.81	7.03	50.1	50.3	0.40	-
R1-n0.2-S	120.29	61.00	2.72	6.80	24.7	55.6	0.20	Strong-axis
R1-n0.4-S	120.29	61.00	2.72	6.80	24.7	55.6	0.40	Strong-axis
R2-n0.2-S	120.21	60.37	1.80	4.51	39.4	85.4	0.20	Strong-axis
R2-n0.4-S	120.21	60.37	1.80	4.51	39.4	85.4	0.40	Strong-axis
R1-n0.2-W	61.00	120.29	2.72	6.80	55.6	24.7	0.20	Weak-axis
R1-n0.4-W	61.00	120.29	2.72	6.80	55.6	24.7	0.40	Weak-axis
R2-n0.2-W	60.37	120.21	1.80	4.51	85.4	39.4	0.20	Weak-axis
R2-n0.4-W	60.37	120.21	1.80	4.51	85.4	39.4	0.40	Weak-axis

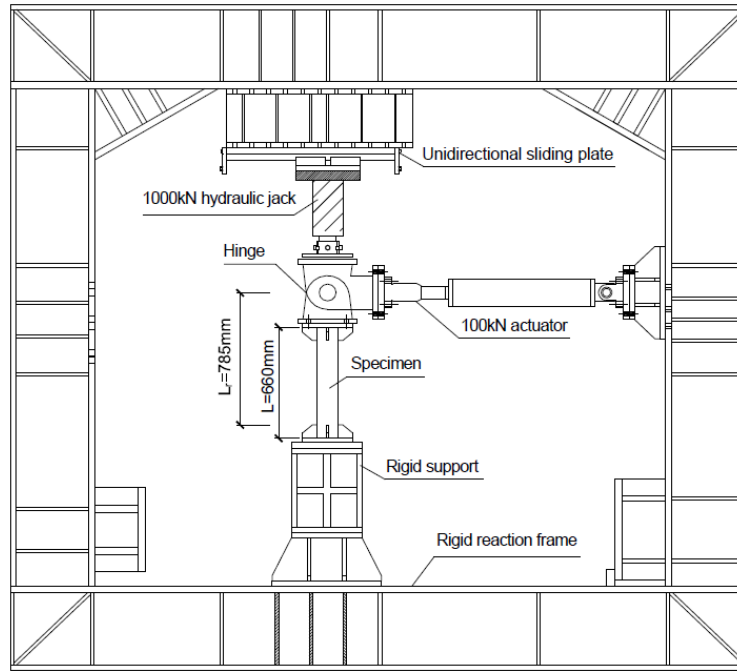
The material properties of the specimens were determined by tensile coupon tests. For each section type, the coupons were taken from the flat part of the three non-welded sides of the tube in the longitudinal direction. The coupons for the material test were cut from the same batch of tube used for producing the specimens. The coupon specimens were prepared in accordance with ISO 6892–1³¹, and they were tested by a MTS testing machine under displacement control. Two strain gauges and a calibrated extensometer of 50 mm gauge length were used to monitor the strain development conditions. The average material properties, including the 0.2% proof stress ($\sigma_{0.2}$), tensile strength (σ_u), Young's modulus (E_0) and elongation after fracture (ε_f), are summarised in Table 2. In addition, the basic Ramberg-Osgood parameter n_f ³², which is obtained from the measured 0.01% and 0.2% proof stresses using the expression of $\ln(0.01/0.2)/\ln(\sigma_{0.01}/\sigma_{0.2})$, is given in the table.

Table 2 Basic material properties

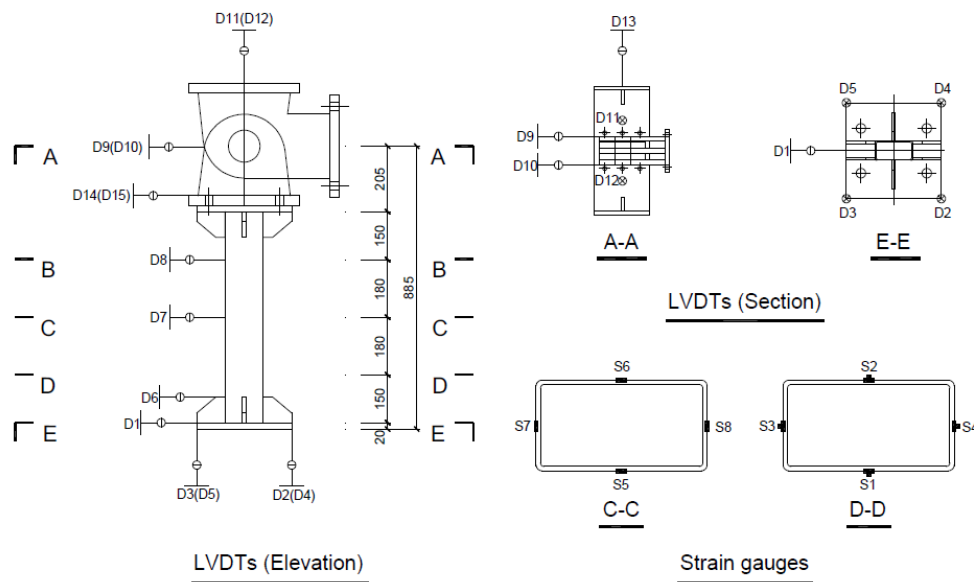
Section	E_0 (GPa)	$\sigma_{0.2}$ (MPa)	σ_u (MPa)	ε_f (%)	n_f
S1	188.5	371.2	851.7	64.6	5.51
R1	189.9	426.2	875.1	55.6	5.01
R2	190.5	407.7	915.7	63.7	5.56

2.2 Test setup, instrumentations, and test procedures

The test setup was arranged such that the specimen acted as a cantilever column with a fixed bottom end and a free top end that can be considered as a contraflexure. The schematic view of the test setup is shown in Fig. 2(a). The bottom end-plate of the specimen was rigidly connected to the strong floor, and the top end-plate was connected to a strong ear plate. The loads were applied to the hinge of the ear plate, such that the top end of the specimen could rotate freely while only the lateral and axial loads could be transferred to the specimen. The loading system consisted of a 100 kN servo-controlled hydraulic actuator to generate the cyclic lateral load and a 1000 kN vertical hydraulic jack to apply the constant axial load. The vertical jack was connected to a sliding device, such that a constant axial compression could reliably exist during the entire test. The out-of-plane displacement at the top of the specimen was prevented via a lateral bracing system.



(a) test setup



(b) instrumentation

Fig. 2 Test arrangement

The applied axial and lateral loads were measured by the load cells of the actuators, and the deformation responses of the specimens were monitored via a series of strain gauges and linear variable differential transformers (LVDTs). The general layout of the instrumentations is shown in Fig. 2(b). The strain gauges were applied in the longitudinal and transverse directions near the bottom stiffeners, a location where local buckling is most likely to occur. Additional longitudinal strain gauges were mounted at the mid-height of the column to check if the vertical load was applied correctly and concentrically. The application of the LVDTs enabled a detailed measurement of the column deformation conditions, including lateral displacement at the loading point, in-plane deflections along the column height, column end shortening, out-of-plane deflection, and the possible source of deformation provided by the bottom end-plate.

The testing procedure included two main steps. The axial load was first applied monotonically onto the specimen and then maintained constant. The cyclic lateral load was subsequently applied with displacement control according to the SAC project recommendation³³, which adopts drift angle as the controlling parameter. The drift angle θ is expressed by $\theta = \Delta/L_r$, where Δ is the lateral displacement recorded at the centre of the hinge of the ear plate, and L_r is the lever arm which is the distance between the hinge and the top of the base stiffeners ($L_r = 785$ mm). The loading drift angle follows the following loading sequences: 0.375% (6 cycles), 0.50% (6 cycles), 0.75% (6 cycles), 1% (4 cycles), 1.5% (2 cycles),

2% (2 cycles), and then continuous at an interval of 1% with two cycles per drift level. The test stopped when the capacity of the actuator was reached, or the moment resistance degraded to 40% of the ultimate moment (M_u).

3 Test Results and Discussions

3.1 Description of failure modes

As expected, no global instability was observed during the entire tests, and local buckling was the governing failure mode for all the specimens. The local failure was featured by the formations of outward or inward bulges that occurred above the base stiffeners, where opposite budging directions were observed for the flanges and webs. The specimens with various section types and axial load ratios seemed to exhibit similar local buckling modes, although the pattern of the bulges may differ due to the uncertainties of initial imperfection. The bending direction was shown to have limited influence on the development sequence of the bulges for RHSs, and it appeared that initial local buckling was always first induced over the more slender constituent plate elements (i.e., those with a larger width-to-thickness ratio). For the specimens with 2 mm-thick tube walls, local buckling could be induced at a very early stage, i.e. 0.375% - 0.5% drifts, whereas for the stockier sections, local buckling normally occurred beyond 1% drift. In addition, a decrease of the axial load ratio could evidently postpone the initiation of local buckling.

Upon the inception of local buckling, the budges developed quickly with increase in drift level, and the bulging area quickly propagated towards the corner of the section. Finally, lateral deformations could be observed at the corner regions themselves, and the specimen completely lost its load carrying capacity. The typical local buckling modes of the specimens at the failure stage are shown in Fig. 3. The development of the bulges was accompanied by gradual column end shortening. The maximum end shortening was less than 10 mm at the failure stage. The out-of-plane displacement recorded near the loading head was less than 1 mm, indicating that the bending action was applied uniaxially. Generally speaking, a more slender section or a higher load ratio resulted in earlier local buckling, and in addition, strong axis bending tended to cause earlier local buckling compared with the case of weak axis bending.

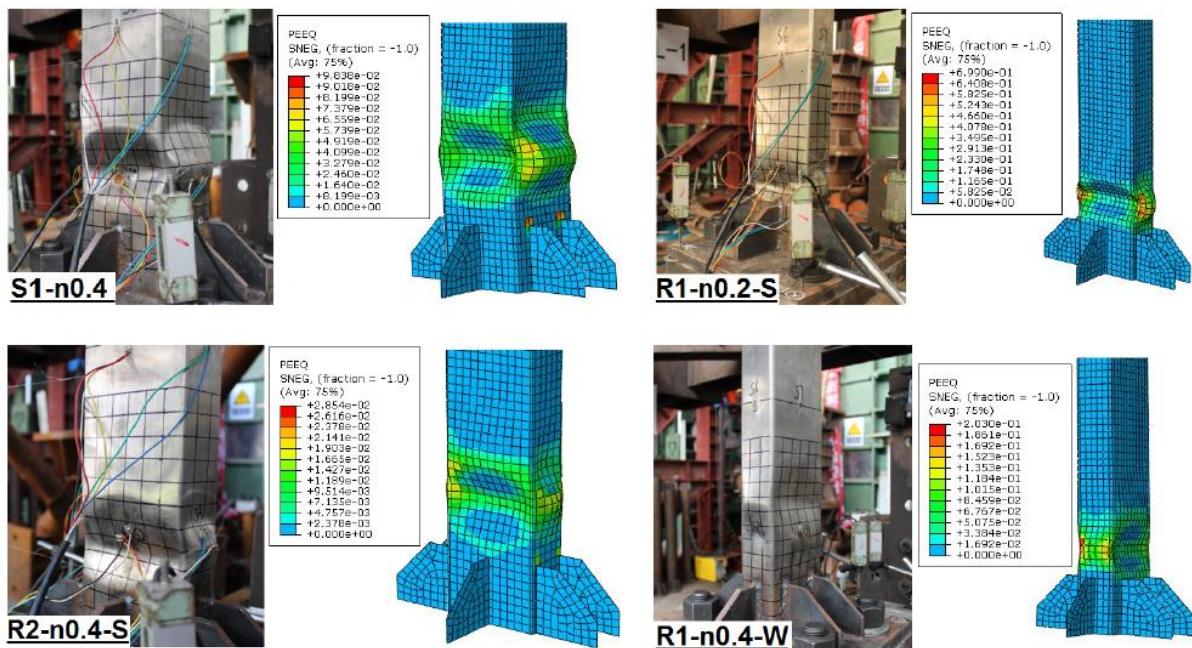


Fig. 3 Typical failure modes and finite element (FE) predictions

3.2 Moment-drift responses

Fig. 4 shows the moment-drift curves of the specimens, where the moment includes both the first-order and second-order effects. The first-order moment was directly caused by the lateral load (V) applied by the horizontal actuator, and is calculated by $M_1 = VL_r$; the second order moment, which resulted from the axial load (P) and lateral displacement (Δ) of the loading head, is expressed by $M_2 = P\Delta$. The results show that the specimens behaved almost linearly prior to 1%-1.5% drift, beyond which inelastic deformation, signified by growing hysteretic loops, started to develop. According to the observed failure modes, it is deduced that the inelastic deformation was mainly provided by the local buckling region near the column base. The specimens can achieve ultimate moment resistance (M_u) ranging from 2.62 kNm to 21.44 kNm. At ultimate moment, the hysteretic response is generally stable, although the shape of the loop is not sufficiently plump, especially for the specimens with a smaller wall thickness. The relatively 'narrow' hysteresis could be due to the less compact sections where local buckling prohibited a full development of the plastic hinge.

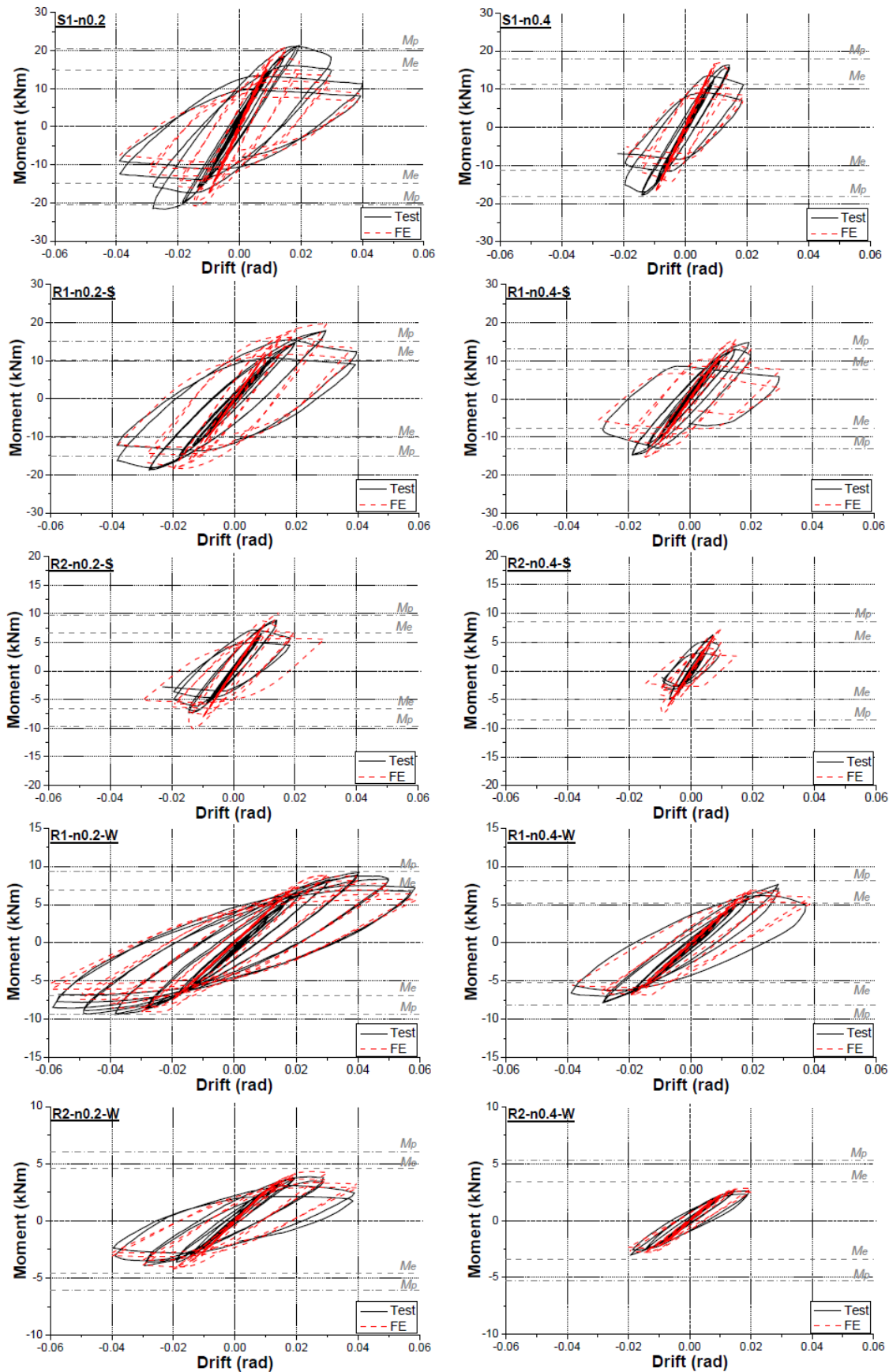


Fig. 4 Moment-drift responses

After achieving the ultimate moment, the moment resistance decreases with increase in drift, i.e., the hysteretic response starts to degrade. With varying section dimensions, axial load ratios, and bending directions, different degradation trends are exhibited. Both the moment resistance and deformation capacity are reduced with decrease in the tube wall thickness. With the same section dimension, the specimens subjected to weak axis bending exhibit higher deformation capacities but reduced ultimate moments compared with those under strong axis bending. This is because of the higher flexural flexibility for the former case. Furthermore, the deformation capacity of the specimens is compromised with increase in axial load ratio, and clearly, this is related to the critical role played by the compressive stress in determining the local buckling performance.

The strength characteristics of the sections can be more clearly reflected by including the elastic moment resistance M_e and plastic moment resistance M_p in Fig. 4. The values of M_e and M_p were calculated using the measured 0.2% proof stress of the flat part, and the effect of the axial force was also taken into account. The comparisons between M_u and M_e (or M_p) can demonstrate the degree of plastic stress development over the section. It is observed that the ultimate moment resistance of specimens R2-n0.2-W and R2-n0.4-W is less than M_e , which indicates that these slender sections subjected to weak axis bending belong to class 4 sections according to the basic definition given by Eurocode 3³⁴. A much more compact behaviour is exhibited by specimens S1-n0.2, R1-n0.2-S, and R1-n0.4-S with less slender sections, where M_p can be achieved but with limited deformability. This suggests that these specimens can be categorized into class 2 sections. For the remaining specimens, M_u falls between M_e and M_p , and therefore they satisfy the criterion of class 3 section.

For stainless steel sections, Eurocode 3² stipulates a detailed classification criterion according to the width-to-thickness ratios of the constituent plate elements under either pure compression (i.e., the case of flange) or combined compression and bending (i.e., the case of web). According to the codified classification limits, the specimens are all class 4 sections with the exception of specimen R1-n0.2-S which belongs to class 3 section. This clearly underestimates the actual section strength. The finding is generally coherent with the conclusion made by Gardner and Theofanous⁹ who gathered and analysed a comprehensive suite of test data on stainless steel sections under compression and bending. The conservatism of the codified treatment for local buckling may be related to the following reasons:

- The interaction of the constituent plate elements is not properly considered.
- The rationality of using the 0.2% proof stress as the yield strength is not fully justified due to the nonlinear stress-strain response of stainless steel with pronounced hardening.
- The enhanced strength of the corner parts was not considered when calculating M_e and M_p .

It should be noted that some of these issues are commonly shared by low carbon steel sections, but some facts may uniquely exist for stainless steel sections. A more detailed discussion on classification of stainless section can be found in the literature⁹, but this is beyond the main focus of the current study.

3.3 Skeleton curves and ductility

Ductility is one of the most essential characteristics when evaluating the seismic performance of steel members. The ductility of the specimens can be conveniently reflected via skeleton curves which are produced according to the moment-drift responses by connecting all the peak drift points at varying cycles. The skeleton curves enable a clear presentation of the initial stiffness, ultimate strength, and post-limit degradation trends of the specimens during the entire loading procedure. As shown in Fig. 5(a), the pattern of the curves greatly depends on the section property, axial load ratio, and bending direction. Based on the responses, the ductility of the specimens can be expressed in a more quantitative manner, i.e., ductility coefficient (μ), which is given by:

$$\mu = \frac{\theta_u}{\theta_y} \quad (1)$$

where θ_y = yield drift, and θ_u = ultimate drift. Currently there is no consistent way to determine the two quantities, but it is commonly accepted that θ_y can be taken as the intersection point between the horizontal line passing through the ultimate moment M_u and the extension line of the initial tangent stiffness, and that θ_u corresponds to the stage when the moment degrades to 85% of M_u ³⁵, as illustrated in Fig. 5(a). According to the definitions, the values of θ_u and θ_y and the associated ductility coefficient μ are summarised in Table 3. Generally speaking, the specimens exhibit low to moderate levels of ductility, where the highest μ is 2.60 for specimen R1-n0.4-W. The lowest μ (i.e., 1.30) is observed in specimen R2-n0.4-S which has a slender section and is subjected to a high axial load ratio. Clearly, the low ductility is due to the early occurrence of local buckling.

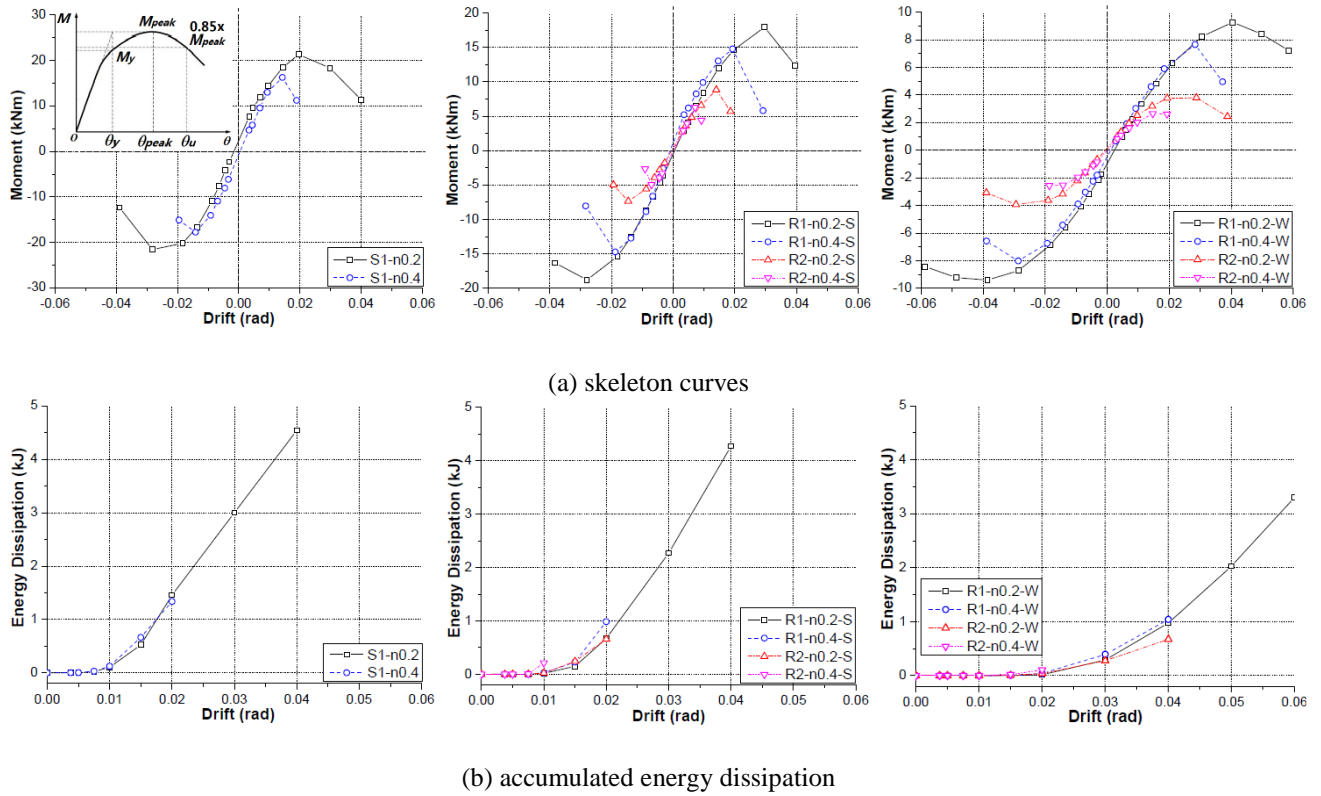


Fig. 5 Further discussions on test results

Alternatively, the ductility or deformability characteristics of steel members can be directly assessed by θ_u , regardless of θ_y . This approach is commonly employed in major codes such as Eurocode 8³⁶ and AISC³⁷. The former requires the rotational capacity of the plastic hinge region being larger than 0.025 radians for structures of ductility class medium (DCM) and being larger than 0.035 radians for structures of ductility class high (DCH); the latter specifies that structures should be able to exhibit inter-story drifts of 2% and 4% for intermediate moment frame (IMF) and special moment frame (SMF), respectively. As the skeleton curves were plotted by the overall drift (rather than the concentrated rotation of the plastic hinge), the AISC criterion is adopted for ductility assessment of the current member. The results show that under an axial load ratio of 0.2, most of the specimens can satisfy the criterion of IMF. One exception is specimen R2-n0.2-S, which has an ultimate drift of only 1.64% when subjected to strong-axis bending. Minor-axis bending could often lead to increased θ_u due to increased member flexibility, and it is noticed that specimen R1-n0.2-W could well achieve the criterion of SMF. When the axial load ratio increases to 0.4, a large number of the specimens fail to meet the IMF criterion. This suggests that the current specimens, especially those with slender sections, may not be suitable for seismic active regions unless a suitably low level of design load ratio is maintained.

3.4 Energy dissipation

In typical steel frames, the input energy is largely dissipated through the inelastic deformation of members that exhibit certain ductility. The dissipated energy of a member under cyclic loading can be quantitatively determined by the area encircled by the hysteretic loops^{38,39}. Fig. 5(b) presents the total accumulated energy dissipation (E_{total}) of the specimens with increase in drift. The results for the SHS specimens and the RHS specimens under strong-axis bending echo their moment-drift responses that limited energy is dissipated at the initial loading stages prior to 1% drift. This low-energy dissipation range can be extended to 1.5%-2% drift for the specimens under weak-axis bending, where increased elastic deformations are available due to a lower flexural rigidity. With the development of inelastic deformation, which leads to growing hysteretic loops, the dissipated energy starts to increase evidently. The final E_{total} prior to failure (i.e. when the moment resistance drops below $0.85M_u$) ranges between approximately 0.2 kJ and 4.5 kJ for the current specimens, and it is confirmed that the energy dissipation is closely related to the ductility characteristic of the specimens. It is found that the specimens with the same section type but under different axial load ratios follow a similar increasing trend of energy dissipation, but the final E_{total} differs significantly as ductility can be compromised by the increase of the load ratio. For the same reason, the energy dissipation capacity of the specimen with a more slender section is significantly suppressed due to early local buckling. The results also show that E_{total} greatly depends on the lateral load resistance of the specimen. Although the specimens under weak-axis bending exhibit better ductility, their E_{total} is not greater than that for the case of strong-axis bending where larger lateral loads have to be applied.

4 Numerical Investigations

4.1 Modelling strategy

To expand upon the limited available experimental data, a numerical investigation was conducted to further discuss the strength and behavior of stainless steel SHSs/RHSs under combined axial and cyclic bending. The numerical models were generated in the commercial finite element (FE) analysis program ABAQUS⁴⁰, as typically shown in Fig. 6. To increase the computational efficiency while maintaining the accuracy of the simulation, only the tube and stiffener parts were modelled, whereas the remaining parts such as the end-plates and ear plate were omitted and replaced by appropriate boundary conditions which were carefully applied to reflect the actual test set up condition. For instance, the column foot including the base stiffeners were applied with a fixed boundary to simulate the welded junction between these parts and the bottom end-plate. The stiffeners were ‘tied’ to the tube wall to simulate the welds. The top part of the tube was fully coupled to a reference point which locates at the same height as that of the loading hinge. The FE model was discretised by 4-node shell elements with reduced integration, i.e., S4R elements in ABAQUS nomenclature, with a meshing size of approximately 10 mm. The measured section dimensions were adopted in the models.

An appropriate representation of the basic material characteristics of stainless steel was considered in the FE models. For the flat part, the measured stress-strain response was directly used, noting that the engineering stress and strain were converted to true stress and strain values. A combined kinematic hardening law was adopted to reflect the cyclic behavior of stainless steel. For the corner part which was not directly tested in the current study, some researchers proposed empirical methods that enable a reasonable representation of the corner stress-strain response based on the knowledge of the flat material properties and other necessary geometric information⁴¹. The enhanced yield strength of the corner part ($\sigma_{0.2,c}$) can be expressed by:

$$\sigma_{0.2,c} = \frac{1.881\sigma_{0.2}}{(r_1/t)^{0.194}} \quad (1)$$

where $\sigma_{0.2}$ is the 0.2% proof stress of the flat part, and r_1 is internal radius of the corner. With the calculated value of $\sigma_{0.2,c}$, the stress-strain relationship of the corner can be represented by a two-stage compound Ramberg-Osgood expression, as given by⁴²:

$$\varepsilon = \begin{cases} \frac{\sigma}{E_{0,c}} + 0.002 \left(\frac{\sigma}{\sigma_{0.2,c}} \right)^{n_c} & \sigma \leq \sigma_{0.2,c} \\ \frac{\sigma - \sigma_{0.2,c}}{E_{0.2,c}} + \varepsilon_{u,c} \left(\frac{\sigma - \sigma_{0.2,c}}{\sigma_{u,c} - \sigma_{0.2,c}} \right)^{m_c} + \varepsilon_{0.2} & \sigma > \sigma_{0.2,c} \end{cases} \quad (2)$$

where

$$E_{0.2,c} = \frac{E_{0,c}}{1 + 0.002n_c E_{0,c} / \sigma_{0.2,c}}, \quad m_c = 1 + 3.5 \frac{\sigma_{0.2,c}}{\sigma_{u,c}}, \quad \sigma_{u,c} = \frac{\sigma_{0.2,c}}{0.2 + 185\sigma_{0.2,c} / E_{0,c}} \quad (3)$$

$$\text{and } \varepsilon_{u,c} = 1 - \frac{\sigma_{0.2,c}}{\sigma_{u,c}}.$$

In the above equations, $E_{0,c}$ and n_c are the Young’s modulus and the Ramberg-Osgood parameter (strain hardening exponent) of the corner part, respectively, which, in the absence of test data, can be taken to be the same as those for the corresponding flat material⁴¹.

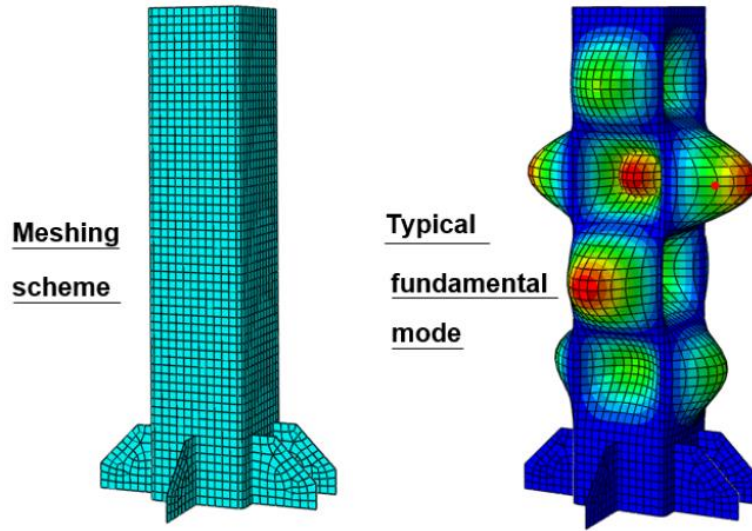


Fig. 6 Typical meshing scheme and fundamental local buckling mode

A characteristic representation of the initial geometric imperfection was considered for the FE models. The pattern of the imperfection shape is based on the fundamental local buckling mode which can be readily obtained through an eigenvalue analysis (buckling analysis) on the model. A uniaxial loading condition was assumed for the eigenvalue analysis, and the typical perturbation shape of the fundamental buckling mode is shown in Fig. 6. The amplitude of this priori defined deformation configuration could be scaled to a desired value. Due to the absence of detailed local imperfection measurement in the current study, an empirical expression proposed by Dawson and Walker⁴³ was consistently adopted in the models:

$$w_0 = 0.023 \left(\frac{\sigma_{0.2}}{\sigma_{cr1}} \right) t \quad (4)$$

where w_0 is the imperfection amplitude, and σ_{cr1} is the elastic critical buckling stress of individual constituent plate element with four edges being simply-supported. For the case of RHS, the value of σ_{cr1} for the flange was considered for calculating σ_{cr1} . Residual stress was not considered in the current models as its influence on the overall response of stainless steel members is deemed to be insignificant⁴⁴. In addition, global imperfection, which is not the focus of this study, was not considered in the model. Incorporating the predetermined local imperfection shape with an appropriate level of amplitude, nonlinear analysis was then performed to obtain the detailed hysteresis and failure responses of the models. The loading protocol was the same as that adopted in the test program.

4.2 Model validation

The above modelling strategy leads to satisfactory agreements between the test results and FE predictions. The pattern and location of local buckling are highly coherent with the test phenomena, as typically shown in Fig. 3. When failure occurs, the models exhibit inward and outward budging patterns near the column base and soon after that the moment resistance starts to degrade and finally to be completely lost. The contour of the equivalent plastic strain (P_{EEQ}) also reveals that the local buckling region has experienced extensive yielding upon failure and thus can contribute to energy dissipation. It is noticed in some models that the predicted pattern of the budges is exactly the opposite of that found in the corresponding specimens, and this is related to the predefined mode of the local buckling waves which could be different from the actual ones. Nevertheless, it is believed that the varied budging directions have little influence on the general section behaviour.

Table 3 Test results and finite element (FE) predictions

Test results							FE predictions					
Specimens	M_u (kNm)	M_u/M_p	M_u/M_e	θ_y (%)	θ_u (%)	μ	M_{u-FE} (kNm)	M_u/M_{u-FE}	θ_{y-FE} (%)	θ_y/θ_{y-FE}	θ_{u-FE} (%)	θ_u/θ_{u-FE}
S1-n0.2	21.44	1.04	1.44	1.40	3.10	2.22	20.83	1.03	1.14	1.23	2.26	1.37
S1-n0.4	17.02	0.94	1.52	1.06	1.80	1.69	16.96	1.00	0.94	1.13	1.53	1.18
R1-n0.2-S	18.38	1.22	1.80	1.84	3.72	2.02	19.11	0.96	1.63	1.13	3.24	1.15
R1-n0.4-S	14.77	1.12	1.93	1.27	2.18	1.72	15.51	0.95	1.33	0.96	1.85	1.18
R2-n0.2-S	8.10	0.83	1.22	1.01	1.64	1.64	9.49	0.85	1.15	0.88	1.73	0.95
R2-n0.4-S	5.63	0.66	1.13	0.62	0.79	1.30	6.15	0.91	0.75	0.82	0.89	0.89
R1-n0.2-W	9.33	1.00	1.35	2.27	5.91	2.60	8.93	1.05	2.35	0.97	4.96	1.19
R1-n0.4-W	7.83	0.96	1.51	1.91	3.47	1.81	6.87	1.14	1.84	1.04	3.81	0.91
R2-n0.2-W	3.86	0.64	0.85	1.49	3.45	2.31	4.22	0.92	1.57	0.95	3.49	0.99
R2-n0.4-W	2.62	0.50	0.77	1.02	1.87	1.84	2.81	0.93	1.06	0.96	2.00	0.94
Mean								0.97		1.01		1.07
CoV								0.079		0.118		0.151

The comparisons between the test and predicted moment-drift responses are given in Fig. 4, and again, satisfactory agreements are shown. The shapes of the hysteretic loops at varying stages are reasonably captured by the FE models, although a certain level of discrepancy is observed in some specimens at the post-limit stage. The discrepancy could arise from the uncertainties related to the initial geometric imperfection as well as the material property at the corner part. Based on the behaviour of the skeleton curves, more detailed comparisons in terms of ultimate moment (M_u), yield drift (θ_y), and ultimate drift (θ_u), are summarised in Table 3. It is observed that the mean test-to-predicted ratios for these quantities range between 0.97 and 1.07, and the associated coefficient of variation (CoVs) range between 0.079 and 0.151. These results are within acceptable ranges from the perspective of engineering application.

5 Parametric Study and Design Considerations

5.1 Parameter matrix and general results

The calibrated FE models enable a further parametric study to be carried out to examine the influence of an extended range of parameters on the cyclic behaviour of stainless steel RHSs/SHSs. A spectrum of section dimensions was considered in the parameter matrix, covering five different tube thicknesses and four section types, as detailed in Table 4. These geometric configurations lead to width-to-thickness ratios ranging from 5.7 to 78.2 for the constituent plate elements of the sections. Both strong-axis and weak-axis bending scenarios were considered, and to facilitate the interpretation of the parametric study results, a shape coefficient (k) is defined as the ratio of the flange width (h) over the web width (b), where $k < 1.0$ indicates that the RHS section is under strong-axis bending, and $k > 1.0$ indicates that the section is under weak-axis bending. The value of k ranges between 0.5 and 2.0 for the current parametric study models. In addition, three practical levels of load ratio were taken into account, i.e. $n = 0.2, 0.4$, and 0.6 . A representative material property, taken from that measured from the flat part of the R1 section, was adopted. The treatment for the corner region was the same as that described in Section 4.1. The other details of the parametric study models, including the boundary conditions and geometric imperfections, are identical to those considered in the calibration models. The parameter matrix leads to a total of 105 models to be built and analysed.

Table 4 Parameter matrix

Parameters	Details
Axial load ratio	0.2, 0.4, 0.6
Tube wall thickness (mm)	3, 4, 6, 8, 10
Section type (mm)	180×90, 180×120, 180×150, 180×180
Bending direction (for RHSs)	Major-axis, Minor-axis
Total number of model	105

Compared with the test specimens, the models show similar trends in terms of strength and ductility with varying section slenderness, bending directions, and axial load ratios. Among all the models, a smallest ultimate moment (M_u) of 5.5 kNm is observed in section 180×90×3 under a load ratio of 0.6 and being subjected to weak-axis bending, and on the other hand, a largest M_u of 278.3 kNm is observed in section 180×180×10 under a load ratio of 0.2. From a ductility point of view, the ultimate drift (θ_u) of the models ranges from 0.3% to 11.2%, and the corresponding ductility coefficient (μ) ranges from 1.00 to 4.68. It should be noted that for very slender sections under a high axial load ratio, local buckling can

occur prior to the application of the lateral load. These sections exhibit almost no ductility, and they can hardly resist any further cyclic loading. In fact, the ‘effective load ratio’ (n_{eff}) for these slender sections is close to 1.0 ($n_{\text{eff}} = P/f_y A_{\text{eff}}$, where A_{eff} is the codified effective cross-sectional area for class 4 sections under pure compression). Although such a high load ratio is very unlikely in practice, these extreme conditions are included in the current study to allow a sufficient range of section slenderness to be considered towards the proposal of design recommendations.

5.2 Design comments on strength

The existing stainless steel codes^{1,2,3, 45} have provided a set of member-level design equations to determine the ultimate strength of beam-columns, and the current numerical results could be useful data to evaluate the rationality of these codified equations. In Eurocode 3², stainless steel beam-columns are designed to satisfy:

$$\frac{N_{\text{Ed}}}{(N_{\text{b,Rd}})_{\text{min}}} + k_y \left(\frac{M_{\text{y,Ed}} + N_{\text{Ed}} e_{\text{Ny}}}{\beta_{\text{w,y}} W_{\text{pl,y}} f_y / \gamma_{\text{M1}}} \right) \leq 1 \quad (5)$$

where N_{Ed} = applied axial load, $(N_{\text{b,Rd}})_{\text{min}}$ = ultimate member buckling resistance under uniaxial compression, $M_{\text{y,Ed}}$ = applied moment, e_{Ny} = loading eccentricity, which is zero for the current case, $\beta_{\text{w,y}} W_{\text{pl,y}}$ = effective section modulus depending on the section classification, f_y = yield strength (0.2% proof stress), k_y = bending-compression interaction factor which is elaborated in Eurocode 3², and γ_{M1} = partial factor. In SEI/ASCE 8-02¹, the strength of in-plane loaded beam-columns are designed according to:

$$\begin{cases} \frac{P_u}{\phi_c P_n} + \frac{C_{\text{my}} M_{\text{uy}}}{\phi_b M_{\text{ny}} \alpha_{\text{ny}}} \leq 1.0 & \frac{P_u}{\phi_c P_n} > 0.15 \\ \frac{P_u}{\phi_c P_n} + \frac{M_{\text{uy}}}{\phi_b M_{\text{ny}}} \leq 1.0 & \frac{P_u}{\phi_c P_n} \leq 0.15 \end{cases} \quad (6)$$

where P_u = applied axial load, P_n = member axial strength, C_{my} = coefficient related to moment distribution and boundary condition, M_{uy} = applied moment, M_{ny} = member flexural strength, $1/\alpha_{\text{ny}}$ = magnification factor, and ϕ_b and ϕ_c = resistance factors. It is noted that the same design equation is considered in AS/NZS4673³. A similar approach is adopted in the Chinese code CECS 410⁴⁵, as given by:

$$\frac{N}{\phi A_e} + \frac{\beta_m M}{(1 - \phi \frac{N}{N_E}) W_e} \leq f \quad (7)$$

where N = applied axial load, ϕ = global buckling coefficient, A_e = effective cross-sectional area, β_m = coefficient related to moment distribution, M = applied moment, N_E = Euler critical load, W_e = effective section modulus, and f = yield strength.

It can be seen that although different terminologies and symbols are employed in different codes, the basic design principles are similar. A more detailed description of the related factors and coefficients is available in the codes, which is not elaborated herein. The above design equations enable a full assessment of the strength of stainless steel beam-column members with both local and global buckling inclusive, although the latter is not a critical issue for the current stub column models. The global buckling reduction coefficients for these stub columns are generally above 0.9. With a fixed load ratio, the design ultimate moments $M_{\text{u,E}}$, $M_{\text{u,A}}$, and $M_{\text{u,C}}$ of the models predicted by Eurocode², SEI/ASCE 8-02¹, and CECS410⁴⁵, respectively, are compared with the FE predictions ($M_{\text{u,FE}}$), as illustrated in Fig. 7. It should be noted that the partial factors (resistance factors) in the design equations were excluded for the calculation of the design ultimate moments.

It is clearly observed that the FE-to-design predicted ratios for nearly all the models are above unity, indicating that the design predictions are on the conservative side. The main reasons for the conservatism have been discussed in Section 3.2. In particular, it may be overly conservative to use the 0.2% proof stress as the design yield strength, since stainless steel exhibits pronounced strain hardening. This also explains the trend that higher FE-to-design predicted ratios are found in more stocky sections which have good ductility and hence adequate developments of section yielding. In addition, ignoring the enhanced material property in the corner region also attributes to the conservative design predictions. However, there are some exceptions where the FE-to-design predicted ratios are below unity. These models have a very slender section ($t = 3$ mm) and a high load ratio ($n = 0.6$), and they are very susceptible to local buckling. This warns that the design predictions could be unsafe for slender sections under combined high axial load ratios and cyclic bending, although this issue may be adequately addressed by considering appropriate partial factors (resistance factors) in design.

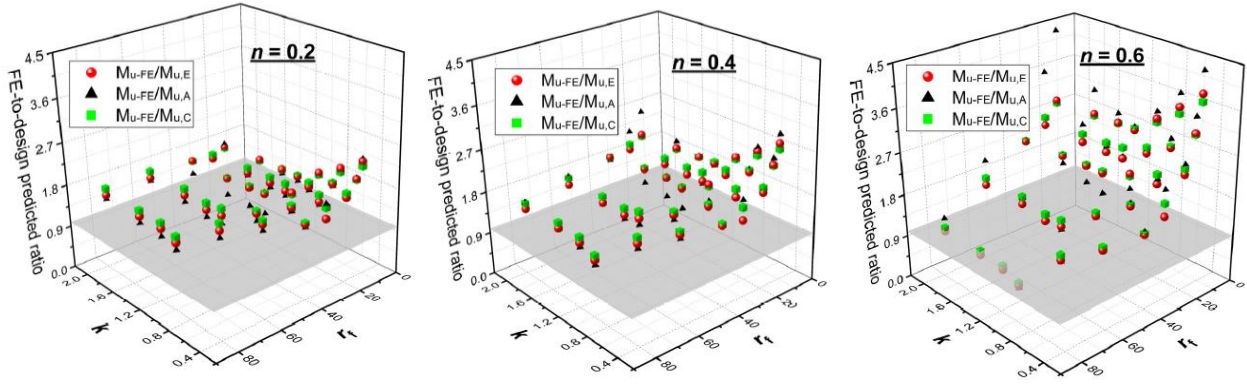


Fig. 7 Comparisons between FE results and codified design predictions

5.3 Ductility-oriented design recommendation

Under the framework of performance-based seismic design approach, ductility is an essential indicator that reflects the performance of structural members against strong earthquakes. Based on the limited numerical data pool, a ductility-oriented design strategy was proposed in order to offer a quick yet reliable evaluation tool for predicting the available ductility supply of stainless steel RHSs/SHSs under different loading conditions. Fig. 8 shows the distributions of ultimate drift (θ_u) with variations of flange width-to-thickness ratio (r_f) and shape coefficient (k) under different axial load ratios, and as aforementioned, θ_u corresponds to the stage when the moment resistance degrades to $0.85M_u$. Being coherent with the test observations, θ_u decreases with increase in r_f , and strong-axis bending (i.e. decrease in k) results in decreased θ_u . In order to reasonably capture these trends, the following set of polynomials were adopted for the prediction of θ_u :

$$\theta_u = \frac{Z_0 + A_0 k + B_0 r_f + B_0 r_f^2 + B_0 r_f^3}{1 + A_1 k + A_2 k^2 + A_3 k^3 + B_1 r_f + B_2 r_f^2} \quad (8)$$

where Z_0 , A series, and B series are constants which change with different loading scenarios and can be derived using nonlinear curve-fitting technique. The values of these constants are summarised in Table 5, and the corresponding matching surfaces are shown in Fig. 8.

Table 5 Constants for design equations

Load ratio	Z_0	A_0	B_0	B_0	B_0	A_1	A_2	A_3	B_1	B_2
0.2	6.08E+01	2.29E+01	-2.74E+00	4.55E-02	-2.75E-04	-1.87E+00	8.88E-01	-1.25E-01	5.09E-02	-3.86E-04
0.4	-5.59E+01	6.77E+02	4.89E+00	-2.63E-01	2.85E-03	-1.41E-01	-4.43E+00	2.17E+00	6.17E-01	6.59E-03
0.6	3.74E+01	-1.28E+02	6.60E-01	-2.84E-02	2.59E-04	-3.75E+00	2.73E+00	-7.18E-01	8.12E-03	-4.56E-03

The proposed design approach leads to a mean FE-to-design predicted ratio of unity, and the associated CoVs are 0.072, 0.098, and 0.092 for the cases of $n = 0.2$, 0.4 and 0.6, respectively. Employing the proposed equation, the section deformability of a stainless steel column under earthquake excitations can be reasonably assessed. For load ratios which fall between the considered range but are not exactly the same as the three specific values, a linear interpolation for θ_u may be conducted. It is worth mentioning that the proposed approach is applicable to the considered range of geometric and material parameters, and caution should be exercised when using the equation for cases beyond the current range. Nevertheless, the form of equation and the design logic can be readily employed in future to cater to an extended range of data when they are available.

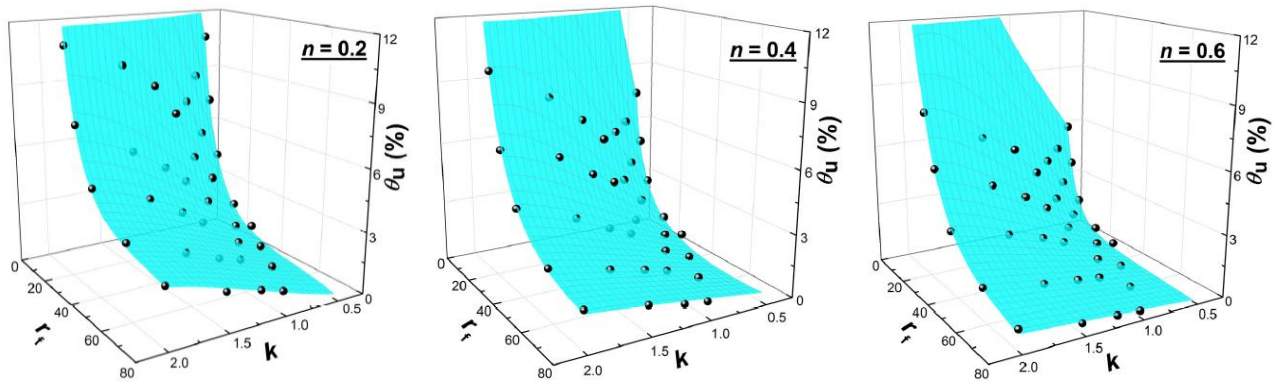


Fig. 8 Ductility-oriented design for prediction of ultimate drift

6 Summary and Conclusions

The behaviour of stainless steel rectangular and square hollow sections (RHSs and SHSs) under combined compression and uniaxial cyclic bending has been discussed in this study. A total of 10 stub column specimens were tested, covering a variety of section slenderness, axial load ratio, and bending direction. A numerical study was subsequently conducted, providing further information on the strength, stress pattern, ductility, and local failure behaviour of the specimens. Adopting the validated numerical modelling approach, a more extensive parametric study was carried out. The results provide basis for the proposal of a ductility-oriented design approach for stainless steel compression members under cyclic loading. The rationality of the current design codes for predicting the strength of stainless steel members was also commented. The main findings and conclusions are noted as follows.

- The failure mode of all the test specimens is governed by local buckling. A slender section is more susceptible to local buckling, and the higher the axial load ratio is, the earlier local buckling tends to occur. Moreover, RHSs under strong-axis bending experiences earlier local buckling compared with those under weak-axis bending, although the location and shape of the bulges seem to be insignificantly influenced by the bending direction.
- Most of the specimens are classified as class 4 sections according to Eurocode 3², but in fact, they could well achieve their elastic moment resistance M_e . This indicates that the current codified classification limits are conservative.
- The specimens exhibit low to moderate levels of ductility, where the ductility coefficient (μ) ranges from 1.30 to 2.60. According to AISC³⁷, the specimens can generally satisfy the criterion of IMF (and possibly SMF), provided that a low axial load ratio (i.e., $n = 0.2$) is applied. When the axial load ratio increases to 0.4, the specimens can hardly meet the IMF criterion. The results suggest that the current specimens may not be suitable for seismic active regions unless a sufficiently low design load ratio is ensured.
- From an energy dissipation point of view, strong-axis bending can lead to more energy dissipation compared with the case of weak-axis bending. Increasing the axial load ratio or section slenderness could compromise the energy dissipation capacity of the specimens due to decreased ductility.
- The parametric study results show that the major design codes provide conservative predictions in terms of the strength of stainless steel beam-columns; the conservatism may be related to inaccurate considerations of constituent plate element interaction, nonlinear stress-strain response of stainless steel, and enhanced strength of the corner parts.
- A ductility-oriented design strategy was proposed to offer a quick yet reliable evaluation tool for predicting the available ductility supply of stainless steel RHSs/SHSs under different loading conditions.

Acknowledgments

Support for this study was provided by a research grant from the State Key Laboratory for Disaster Prevention in Civil Engineering (Grant No. SLDRCE14-B-07). The financial support from the ‘Program for Young Excellent Talents in Tongji University’ is also gratefully acknowledged.

References

- 1 SEI/ASCE 8-02, Specification for the Design of Cold-formed Stainless Steel Structural Members, American Society of Civil Engineers (ASCE), Reston, 2002.
- 2 EN 1993-1-4, Eurocode 3: Design of Steel Structures – Part 1–4: General Rules–Supplementary Rules for Stainless Steels, European Committee for Standardisation (CEN), Brussels, 2006.
- 3 AS/NZS4673, Cold-formed Stainless Steel Structures, Sydney, AS/NZS4673:2001, 2001.
- 4 Baddoo NR. Stainless steel in construction: A review of research, applications, challenges and opportunities. Journal of Constructional Steel Research 2008;64:1199–206.

- 5 Young B, Lui WM. Behaviour of cold-formed high strength stainless steel sections. *Journal of Structural Engineering* 2005;131(11):1738–45.
- 6 Gardner L, Nethercot DA. Experiments on stainless steel hollow sections, Part 1: Material and cross-sectional behaviour. *Journal of Constructional Steel Research* 2004;60(9):1291–318.
- 7 Bardi FC, Kyriakides S. Plastic buckling of circular tubes under axial compression-part I: Experiments. *International Journal of Mechanical Sciences* 2006;48(8):830–41.
- 8 Zhou F, Chen YY, Young B. Cold-formed high strength stainless steel cross-sections in compression considering interaction effects of constituent plate elements. *Journal of Constructional Steel Research* 2013;80:32–41.
- 9 Gardner L, Theofanous M. Discrete and continuous treatment of local buckling in stainless steel elements. *Journal of Constructional Steel Research* 2008;64:1207–16.
- 10 Rasmussen KJR, Hancock GJ. Design of cold-formed stainless steel tubular members. I: Columns. *Journal of Structural Engineering, ASCE* 1993;119(8):2349–67.
- 11 Young B, Liu Y. Experimental investigation of cold-formed stainless steel columns. *Journal of Structural Engineering, ASCE* 2003;129(2):169–76.
- 12 Liu Y, Young B. Buckling of stainless steel square hollow section compression members. *Journal of Constructional Steel Research* 2003;59(2):165–77.
- 13 Theofanous M, Gardner L. Testing and numerical modelling of lean duplex stainless steel hollow section columns. *Engineering Structures* 2009;31:3047–58.
- 14 Real E, Mirambell E. Flexural behaviour of stainless steel beams. *Engineering Structures* 2005;27(10):1465–75.
- 15 Gardner L, Nethercot DA. Experiments on stainless steel hollow sections, Part 2: Member behaviour of columns and beams. *Journal of Constructional Steel Research* 2004;60(9):1319–32.
- 16 Zhou F, Young B. Tests of cold-formed stainless steel tubular flexural members. *Thin-Walled Structures* 2005;43(9):1325–37.
- 17 Huang Y, Young B. Experimental investigation of cold-formed lean duplex stainless steel beam-columns. *Thin-Walled Structures* 2014;76:105–17.
- 18 Lui WM, Ashraf M, Young B. Tests of cold-formed duplex stainless steel SHS beam-columns. *Engineering Structures* 2014;74:111–21.
- 19 Arrayago I, Picci F, Mirambell E, Real E. Interaction of bending and axial load for ferritic stainless steel RHS columns. *Thin-Walled Structures* 2015;91:96–107.
- 20 Arrayago I, Real E, Mirambell E. Experimental study on ferritic stainless steel RHS and SHS beam-columns. *Thin-Walled Structures* 2016;100:93–104.
- 21 Zheng BF, Hua X, Shu GP. Tests of cold-formed and welded stainless steel beam-columns. *Journal of Constructional Steel Research* 2015;111:1–10.
- 22 Zhao O, Gardner L, Young B. Testing and numerical modelling of austenitic stainless steel CHS beam-columns. *Engineering Structures* 2016;111:263–74.
- 23 Zhao O, Gardner L, Young B. Behaviour and design of stainless steel SHS and RHS beam-columns. *Thin-Walled Structures* 2016;106:330–45.
- 24 Uy B, Tao Z, Han LH. Behaviour of short and slender concrete-filled stainless steel tubular columns. *Journal of Constructional Steel Research* 2011;67(3):360–78.
- 25 Uy B, Tao Z, Han LH. Behaviour of short and slender concrete-filled stainless steel tubular columns. *Journal of Constructional Steel Research* 2011;67(3):360–78. [25] Han LH, Chen F, Liao FY, Tao Z, Uy B. Fire performance of concrete filled stainless steel tubular columns. *Engineering Structures* 2013; 56:165–81.
- 26 Tao Z, Ghannam M, Song TY, Han LH. Experimental and numerical investigation of concrete-filled stainless steel columns exposed to fire. *Journal of Constructional Steel Research* 2016;118:120–34.
- 27 Hassanein MF, Elchalakani M, Patel VI. Overall buckling behaviour of circular concrete-filled dual steel tubular columns with stainless steel external tubes. *Thin-Walled Structures* 2017;115:336–48.
- 28 Chen Y, Feng R, Wang LP. Flexural behaviour of concrete-filled stainless steel SHS and RHS tubes. *Engineering Structures* 2017;134:159–71.
- 29 Nip KH, Gardner L, Davies CM, Elghazouli AY. Extremely low cycle fatigue tests on structural carbon steel and stainless steel, *Journal of Constructional Steel Research* 2010;66(1):96–110.
- 30 Zhou F, Li L. Experimental study on hysteretic behaviour of structural stainless steels under cyclic loading. *Journal of Constructional Steel Research* 2016;122:94–109.

- 31 International Organisation for Standardisation (ISO). Metallic Materials — Tensile Testing—Part 1: Method of Test at Room Temperature, ISO 6892-1, London, British, 2009.
- 32 Ramberg W, Osgood WR. Description of stress strain curves by three parameters. Technical Note No. 902. Washington, DC: National Advisory Committee for Aeronautics; 1943.
- 33 Clark P, Frank K, Krawinkler H, Shaw R. Protocol for fabrication, inspection, testing, and documentation of beam-column connection tests and other experimental specimens, SAC Report SAC/BD-97/02, SAC Joint Venture, 1997.
- 34 EN 1993-1-1:2005, Eurocode 3: Design of steel structures – Part 1-1: General rules and rules for buildings. European Committee for standardisation, Brussels, Belgium, 2005.
- 35 Wang W, Fang C, Chen YY, Wang MX. Seismic performance of steel H-beam to SHS-column cast modular panel zone joints. *Engineering Structures* 2016;117:145–60.
- 36 EN 1998-1:2004, Eurocode 8: Design of structures for earthquake resistance – Part 1: General rules, seismic actions and rules for buildings. Brussels, Belgium, 2004.
- 37 AISC 2010, Seismic provisions for structural steel buildings. American Institute of Steel Construction, Chicago, IL, USA, 2010.
- 38 Fang C, Yam MCH, Lam ACC, Xie LK. Cyclic performance of extended end-plate connections equipped with shape memory alloy bolts. *Journal of Constructional Steel Research* 2014;94:122–36.
- 39 Yam MCH, Fang C, Lam ACC, Zhang YY. Numerical study and practical design of beam-to-column connections with shape memory alloys. *Journal of Constructional Steel Research* 2015;104:177–92.
- 40 ABAQUS Analysis User's Manual, ABAQUS Standard, Version 6.10.
- 41 Ashraf M, Gardner L, Nethercot D A. Finite element modelling of structural stainless steel cross-sections. *Thin-walled structures* 2006;44(10):1048–62.
- 42 Rasmussen KJR. Full-range stress–strain curves for stainless steel alloys. *Journal of Constructional Steel Research* 2003;59:47–61.
- 43 Dawson RG, Walker AC. Post-buckling of geometrically imperfect plates. *Journal of the Structural Division ASCE* 1972; 98:ST1:75–94.
- 44 Huang Y, Young B. Experimental and numerical investigation of cold-formed lean duplex stainless steel flexural members. *Steel Construction* 2014;73(4):216–28.
- 45 CECS 410:2015 Technical specification for stainless steel structure. Beijing: China Planning Press, 2015 (in Chinese).